

## STELLAR VELOCITY DISPERSION AND ANISOTROPY OF THE MILKY WAY INNER HALO

CHARLES KING III<sup>1</sup>, WARREN R. BROWN, MARGARET J. GELLER, SCOTT J. KENYON  
Smithsonian Astrophysical Observatory, 60 Garden Street, Cambridge, MA 02138  
*Draft version March 2, 2024*

## ABSTRACT

We measure the three components of velocity dispersion,  $\sigma_R, \sigma_\theta, \sigma_\phi$ , for stars within  $6 < R < 30$  kpc of the Milky Way using a new radial velocity sample from the MMT telescope. We combine our measurements with previously published data so that we can more finely sample the stellar halo. We use a maximum likelihood statistical method for estimating mean velocities, dispersions, and covariances assuming only that velocities are normally distributed. The alignment of the velocity ellipsoid is consistent with a spherically symmetric gravitational potential. From the spherical Jeans equation, the mass of the Milky Way is  $M(R \leq 12 \text{ kpc}) = 1.3 \times 10^{11} M_\odot$  with an uncertainty of 40%. We also find a region of discontinuity,  $15 \lesssim R \lesssim 25$  kpc, where the estimated velocity dispersions and anisotropies diverge from their anticipated values, confirming the break observed by others. We argue that this break in anisotropy is physically explained by coherent stellar velocity structure in the halo, such as the Sgr stream. To significantly improve our understanding of halo kinematics will require combining radial velocities with future *Gaia* proper motions.

*Subject headings:* Galaxy: fundamental parameters — Galaxy: halo — Galaxy: structure — Galaxy: kinematics and dynamics — Galaxy: formation — stars: Population II

## 1. INTRODUCTION

The global kinematics of halo stars encodes important information about the mass, structure, and formation of the Milky Way. The existence of coherent structures, such as the Sgr tidal stream (Ibata et al. 1994; Majewski et al. 2003), demonstrates that at least part of the Milky Way halo emerged from the accretion of smaller galaxies as expected in hierarchical galaxy formation (e.g., Searle & Zinn 1978). Theoretical simulations suggest that the inner  $R \lesssim 20$  kpc region of the stellar halo should be dominated by stars formed *in situ* whereas the outer region should be dominated by accreted stars on increasingly radial orbits (Bullock & Johnston 2005; Abadi et al. 2006; Johnston et al. 2008; Zolotov et al. 2009; Font et al. 2011; McCarthy et al. 2012; Rashkov et al. 2013).

Modern studies based on observational data from the Sloan Digital Sky Survey (SDSS) support a dual component stellar halo (Carollo et al. 2007, 2010; Beers et al. 2012). In this view, the inner halo  $R < 15$  kpc exhibits a flattened distribution of stars on radial orbits with no net rotation contrasted with the outer halo  $R > 20$  kpc characterized by a spherical distribution of stars with net retrograde rotation. Schönrich et al. (2011, 2014), however, argue that the dual halo results from observational errors and selection effects, and cannot be distinguished from a single halo full of substructure.

Intiguently, many other observers find a discontinuity in both the number density and the orbital properties of halo stars near  $R \simeq 20$  kpc. Star counts of main sequence turn-off stars (Bell et al. 2008; Sesar et al. 2011), RR Lyrae stars (Watkins et al. 2009; Sesar et al. 2013), blue horizontal branch (BHB) stars (Deason et al. 2011), and K giants (Kafle et al. 2014) all exhibit a break in the

number density around  $R = 16 - 26$  kpc. Radial velocity surveys of BHB stars imply systematically radial orbits in the inner and outer halo (Deason et al. 2011, 2012) but more tangential orbits in the region  $15 < R < 25$  kpc (Kafle et al. 2012; Deason et al. 2013). The anisotropy,  $\beta$ , that depends on the ratio of tangential and radial velocity dispersions, provides a useful means for quantifying systematic velocity changes in the break region.

Several studies have exploited large samples of halo stars to measure the velocity dispersion and anisotropy profiles beyond  $R > 10$  kpc with varying results. Sirko et al. (2004) employed a sample of 1,170 BHB stars selected from the SDSS Data Release 4 to measure the anisotropy  $\beta = 0.1 \pm 0.2$ , a result consistent with isotropy, for stars with a median distance from the Galactic center of  $R \sim 25$  kpc. Deason et al. (2012) analyzed 1,933 BHB stars from SDSS Data Release 8 (DR8) with  $16 < R < 48$  kpc to find a radially biased anisotropy of  $\beta = 0.5^{+0.08}_{-0.2}$ . Looking for evidence of a multi-component halo, Kafle et al. (2012) analyzed an SDSS DR8 sample of about 4,500 BHB stars and found the anisotropy was radially biased,  $\beta = 0.5$ , for  $9 < R < 12$  kpc and  $25 < R < 56$  kpc. To their astonishment, they discovered a sharp dip,  $\beta \sim -1.2$ , in the anisotropy parameter profile at  $R \simeq 17$  kpc that they could not explain as arising either from halo substructures or from accretion.

Stellar velocities also provide information about the gravitational potential and mass of the Galaxy. The spherical Jeans (1915) equation provides a quantitative link between observations and the underlying gravitational potential (e.g., Binney & Tremaine 2008). Several sophisticated Jean analyses have been performed in recent years, exploring the importance of density profiles, anisotropy assumptions, and potential models with SDSS observations (Deason et al. 2012; Kafle et al. 2012, 2014; Loebman et al. 2014). This paper explores the kinematics of stars with  $6 < R < 30$  kpc using new and existing

cking@cfa.harvard.edu, wbrown@cfa.harvard.edu

<sup>1</sup> Pleiades Consulting Group, Inc., P.O. Box 531, Lincoln, MA 01773

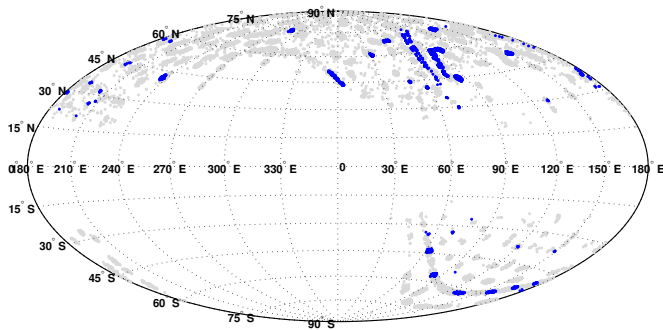


FIG. 1.— Angular distribution of F stars in the Hectospec (blue) and SDSS (gray) surveys in Galactic latitude and longitude. The SDSS BHB stars have essentially the same footprint as the SDSS F stars (gray).

data sets.

We present a spectroscopic radial velocity survey of 6,174 faint  $18 < r < 21$  F-type stars obtained with the Hectospec spectrograph on the 6.5m MMT telescope. We target F-type stars because they are the densest luminous stellar tracer at heliocentric distances of 12 to 20 kpc. Padova tracks predict that a 10 Gyr old  $0.8 M_{\odot}$  star with  $[\text{Fe}/\text{H}] = -1.7$  has an absolute magnitude of  $M_r = +4.5$  (Girardi et al. 2002; Marigo et al. 2008; Bressan et al. 2012), a value consistent with globular cluster observations (Newby et al. 2011). Thus  $r = 20$  and 21 mag F-type stars probe the halo at 12 and 20 kpc heliocentric distances, respectively. To validate our results and improve our statistics, we also make use of 13,480 F-type stars culled from the SDSS. Because the SDSS F star sample is shallower than our Hectospec F star sample, we also use 3,330 BHB stars culled from the SDSS to better constrain the more distant region  $R > 15$  kpc.

In the next section, we describe the three data sets used in our analyses. Section 3 discusses the geometry of projecting the components of velocity on the line of sight and develops maximum likelihood statistical methods to infer the distribution of velocities from the observed line-of-sight velocities. Section 4 describes the mean velocity, dispersion, covariance, and anisotropy profiles; the tilt of the velocity ellipsoid; and the mass of the Galaxy. In Section 5, we test the assumption of independent, normally distributed velocities and investigate the potential effect of the non-normal velocity distribution of the Sgr stream on our analysis. We summarize our conclusions in Section 6.

## 2. DATA

We analyze three data sets, including a new sample of radial velocities obtained with the Hectospec spectrograph on the 6.5m MMT telescope. To validate our results and improve our statistics, we add F-type stars culled from the SDSS Stellar Parameter Pipeline (SSPP, Lee et al. 2008; Allende Prieto et al. 2008) and the BHB star sample of Xue et al. (2011).

### 2.1. Hectospec F Star Sample

#### 2.1.1. Observations

Hectospec is a 300 fiber, multi-object spectrograph with a 1 degree diameter field of view on the 6.5m MMT telescope (Fabricant et al. 2005). All observations are

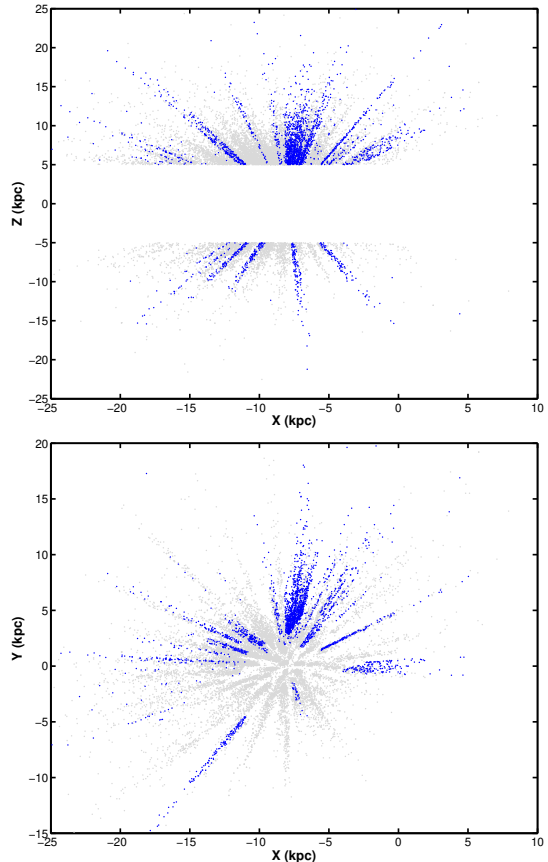


FIG. 2.— Spatial distribution of F stars in the Hectospec (blue) and SDSS (gray) surveys projected onto the Galactic Cartesian coordinate X-Z and X-Y planes. The Sun is located at  $X = -8$  kpc.

made with the 270 line  $\text{mm}^{-1}$  grating, which provides a spectral resolution of  $5 \text{ \AA}$  over the spectral range 3700 – 9100  $\text{\AA}$ . Hectospec fibers are assigned such that high priority targets are assigned first, followed by lower priority targets. All targets and their priorities are determined on the basis of SDSS de-reddened (Schlegel et al. 1998) point spread function magnitudes and colors. We indicate de-reddened magnitudes and colors with a subscript 0.

We acquired 3,197 spectra between 2004 April and 2005 July, the first year of Hectospec operations, with a dedicated halo star observing program. Our dedicated program targeted  $17 < g_0 < 20$  mag stars, prioritizing A-type (candidate BHB) stars and filling the remaining Hectospec fibers with increasingly red stars out to  $(g - r)_0 < 0.5$ . Given the relative surface densities of stars, 80% of the targets were F-type stars.

We acquired an additional 8,143 spectra between 2009 January and 2015 July with a parallel Hectospec observing program. Our parallel program took advantage of all unassigned fibers in Smithsonian Astrophysical Observatory (SAO) Hectospec programs, and filled those fibers with  $18 < r_0 < 21$  F-type stars. Our target selection for the parallel program prioritized the faintest stars at the main sequence turn-off  $(g - r)_0 \simeq 0.25$ . The parallel program yielded between 200 and 2,000 spectra a year, depending on fiber availability and Hectospec usage.

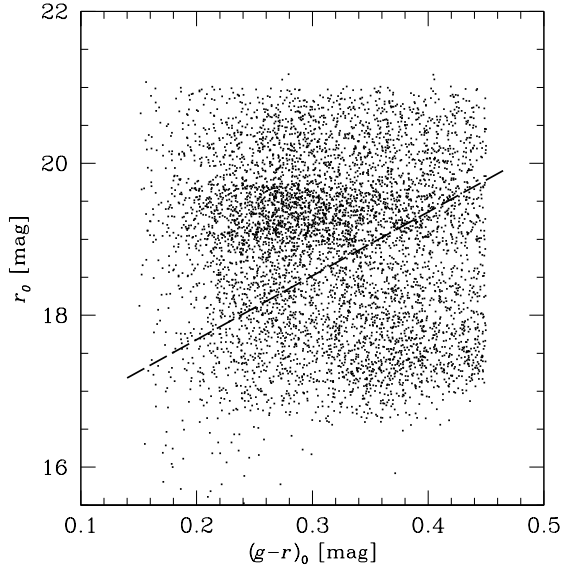


FIG. 3.— Color-magnitude distribution of the Hectospec sample of 6,174 F-type stars. All photometry comes from SDSS de-reddened point spread function magnitudes. The median depth is  $r_0 = 19.0$ , or 8 kpc. Applying a  $|Z| > 5$  kpc cut removes the stars approximately below the dashed line.

Given the nature of our parallel observations, the overall angular distribution of F stars is irregular and clumpy, as seen in Figures 1 and 2. The inner stellar halo of the Milky Way is expected to be spatially well-mixed, however (Bullock & Johnston 2005). Thus the F stars, selected by color, should be fair probes of halo kinematics.

### 2.1.2. Radial Velocities

All Hectospec spectra are processed by the SAO Telescope Data Center’s data reduction pipeline (Mink et al. 2007). We visually inspect each spectrum for quality control. The major contaminants are M-type stars (4% of the spectra) and quasars and miscellaneous galaxies (1% of the spectra). All contaminants are removed from the final Hectospec sample.

We measure stellar radial velocities with the RVSAO cross correlation package (Kurtz & Mink 1998). We use cross-correlation templates constructed from Hectospec observations of 33 bright A- and F-type stars with known velocities from the Century Survey Galactic Halo Project (Brown et al. 2003, 2005b, 2008). We adopt the weighted mean velocity for objects with more than one observation (7% of the spectra). Our median radial velocity uncertainty is  $\pm 15$  km s $^{-1}$  for  $r_0 = 20$  mag F-type stars.

A cross-identification search finds 566 spectra in common with the SDSS SSPP catalog. The mean difference between our radial velocity and SSPP *elodieru*final is  $1.0 \pm 20.4$  km s $^{-1}$ . Our systematic error with respect to SDSS is thus 1 km s $^{-1}$ , which is consistent with the sum of the measurement uncertainties.

### 2.1.3. Final Sample

Our targets were selected from a variety of SDSS data releases. We unify the photometry for this paper using SDSS Data Release 10 de-reddened point spread function magnitudes and colors. Figure 3 presents a color-magnitude plot of the cleaned Hectospec sample, which has a median depth of  $r_0 = 19.0$  mag.

Our spectra were acquired with a variety of exposure times and observing conditions. We therefore remove low quality observations as the first step of making a clean sample. We require that each spectrum has more than 60 instrumental counts and a signal-to-noise ratio per pixel  $(S/N) > 4$  in the continuum at 5000 Å. Radial velocity measurements are possible from lower quality spectra, but our S/N requirement ensures repeatable velocities with  $\leq 40$  km s $^{-1}$  errors. Second, we require that the ratio of counts in the continuum at 7800 Å and 5000 Å is  $< 1.25$ . This requirement, given the Hectospec grating blaze function, eliminates all non-stellar objects, such as quasars, and spurious red objects, such as M-type stars. Finally, we impose  $0.15 < (g-r)_0 < 0.45$  and  $0.4 < (u-g)_0 < 1.4$  to yield a clean sample of 6,174 F-type stars.

Given the low spectral resolution and modest S/N ratio of the Hectospec spectra, we do not perform stellar atmosphere model fits. Instead, we use the Ivezić et al. (2008) photometric parallax relation in combination with the Bond et al. (2010) metallicity calibration. These relations use de-reddened broadband *ugri* colors to estimate stellar luminosity  $M_r$  and metallicity  $[\text{Fe}/\text{H}]$ . Our radial velocity cross-correlation templates span A through F spectral types, and the best-matching template to each spectrum validates this approach.

The average  $[\text{Fe}/\text{H}] = -1.4$  and  $M_r = +4.5$  for our entire sample are consistent with expectations of halo F-type stars (Ivezić et al. 2008; Bond et al. 2010). At faint  $r > 19$  magnitudes and low S/N ratio, however, the scatter in our estimated  $[\text{Fe}/\text{H}]$  becomes implausibly large. Spectroscopic metallicity measurements show that F-type stars at these depths have  $-3 < [\text{Fe}/\text{H}] < -1$  and mean  $[\text{Fe}/\text{H}] = -1.6$  (Allende Prieto et al. 2014). To minimize the distance error for stars with poorly estimated  $[\text{Fe}/\text{H}]$ , we assign  $[\text{Fe}/\text{H}] = -1.6$  to stars with  $[\text{Fe}/\text{H}] < -3$  or  $[\text{Fe}/\text{H}] > -1$ . We expect that our distance estimates are precise to about 15% (Ivezić et al. 2008; Bond et al. 2010). Our measured heliocentric radial velocities and estimated distances are provided in the Appendix A.3.

To remove all significant disk contamination, we impose  $|Z| > 5$  kpc. This cut is motivated by the observed distributions of velocity and metallicity for F stars, which show that the disk population becomes negligible around  $|Z| = 4 - 5$  kpc (Ivezić et al. 2008; Carollo et al. 2010; Bond et al. 2010; Fermani & Schönrich 2013). Restricting the sample to stars with Galactic rest frame velocities  $|v_{rf}| < 500$  km s $^{-1}$  to eliminate potential unbound hypervelocity stars (Brown et al. 2005a) does not remove any stars from the sample. Our final Hectospec sample contains 3,049 F-type stars.

## 2.2. SDSS F Star Sample

The SSPP catalog provides spectroscopic measures of effective temperature, surface gravity, and metallicity for stars observed by SDSS (Lee et al. 2008; Allende Prieto et al. 2008). We construct an F star sample from the SSPP catalog by selecting stars that have a stellar classification of F and extinction corrected colors satisfying  $0.4 < (u-g)_0 < 1.4$ ,  $0.15 < (g-r)_0 < 0.45$ , and  $-0.2 < (r-i)_0 < 0.6$ . We estimate heliocentric distances using the Ivezić et al. (2008) photometric parallax

relation for consistency with the Hectospec sample. The median depth of the resulting F star sample is  $r_0 = 17.4$ , or  $d \simeq 4$  kpc.

Requiring  $|v_{rf}| < 500$  km s $^{-1}$  to avoid potential contamination by hypervelocity stars removes five stars, all of which have large radial velocity errors. Removing all objects in common with the clean Hectospec F-star sample and performing a cut  $|Z| > 5$  kpc to remove potential disk contaminants yields a sample of 13,480 stars. The median heliocentric radial velocity uncertainty is  $\pm 11$  km s $^{-1}$  for  $r = 20$  mag F stars.

Figure 1 compares the angular distribution of the Hectospec and SDSS F star samples on the sky. The overall distribution reflects the SDSS imaging footprint, which covers a large range of Galactic longitude but a restricted range of Galactic latitude, convolved with the spectroscopic survey regions. Figure 2 displays the corresponding spatial distribution of these stars projected onto X-Y and X-Z planes in Galactic Cartesian coordinates. The majority of F stars are within about 10 kpc of the Sun and densely probe out to  $R \simeq 20$  kpc Galactocentric distances.

### 2.3. SDSS BHB Star Sample

Xue et al. (2011) spectroscopically identify 4,985 stars in SDSS as luminous BHB stars. These objects are evolved, metal-poor halo stars with typical absolute magnitudes of  $M_g \simeq +0.8$  mag, significantly more luminous than the F-type stars. Because the BHB stars come from SDSS spectroscopic fields, the sky coverage is essentially identical to that of the SDSS F star sample (Figure 1).

We estimate BHB absolute magnitudes and distances using the Deason et al. (2011) color-magnitude relation. The median apparent magnitude of the BHB sample is  $g_0 = 16.7$  mag, corresponding to a depth of 15 kpc. Imposing a restriction on velocity that  $|v_{rf}| < 500$  km s $^{-1}$  to avoid potential contamination by hypervelocity stars does not eliminate any stars. Retaining only stars with  $|Z| > 5$  kpc to avoid disk contamination yields a sample of 3,330 stars. The median heliocentric radial velocity uncertainty is  $\pm 9$  km s $^{-1}$  for  $g = 19$  mag BHB stars.

### 2.4. Galactic Rest Frame Velocity

We transform all heliocentric velocities,  $v_{helio}$ , to Galactocentric rest frame velocities,  $v_{rf}$ , assuming a circular velocity of 235 km s $^{-1}$  (Reid et al. 2009; McMillan & Binney 2010; Bovy et al. 2012; Reid et al. 2014) and a solar motion of  $(U, V, W) = (11.1, 12.24, 7.5)$  km s $^{-1}$  (Schönrich et al. 2010),

$$v_{rf} = v_{helio} + 235 \sin(l) \cos(b) + 11.1 \cos(l) \cos(b) + 12.24 \sin(l) \cos(b) + 7.25 \sin(b). \quad (1)$$

Figure 4 plots summary statistics for the observed  $v_{rf}$  distribution for the combined data sets. We use bins of fixed 4 kpc width and plot points at the mean  $R$  of each bin. Figure 4 (panel a) shows that the velocity dispersion of the combined data sets is relatively constant except for the range  $15 < R < 18$  kpc, where the velocity dispersion declines suddenly from 123 km s $^{-1}$  to 102 km s $^{-1}$ . Interestingly, the Hypervelocity Star survey measures a  $113.9 \pm 6.6$  km s $^{-1}$  velocity dispersion  $15 < R < 20$  kpc (Brown et al. 2010) in perfect agreement with the average velocity dispersion in this region.

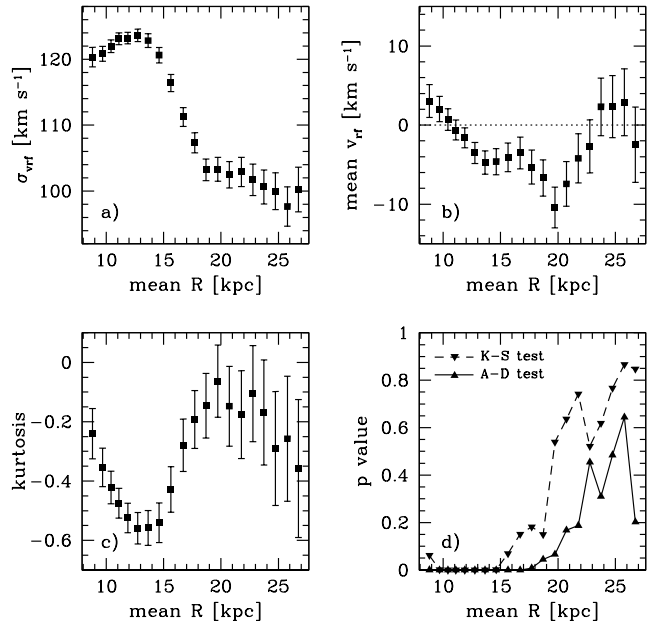


FIG. 4.— Statistics of the observed  $v_{rf}$  distribution for the combined sample versus the mean  $R$  for each bin. Bins have fixed 4 kpc width and thus overlap in  $R$ , with varying number of stars per bin. Panel a) is the velocity dispersion, panel b) is the mean velocity, panel c) is the kurtosis, and panel d) is the  $p$  value of Kolmogorov-Smirnoff (K-S) and Anderson-Darling (A-D) tests for normality of the  $v_{rf}$  distributions in each bin.

Figure 4 (panel b) shows some apparent variation in the mean velocity of the stars, but for most bins the mean velocity does not differ significantly from 0 km s $^{-1}$ . Figure 4 (panel c) shows that the kurtosis of the distribution differs significantly from zero, however, indicating that the distribution of  $v_{rf}$  departs from a normal distribution for bins  $R < 18$  kpc. Both Kolmogorov-Smirnoff and Anderson-Darling tests significantly reject a normal distribution for bins  $R < 18$  kpc. We caution that both statistical tests are sensitive to the number of stars and note that the outer bins contain many fewer stars than the inner bins.

## 3. THEORY AND METHODOLOGY

There are few tests of the dynamical models used to derive Galactic parameters. Halo models typically postulate a high degree of spatial symmetry and assume that the velocities of halo stars are normally distributed and uncorrelated with zero means. The presence of structure and star streams expected in hierarchical galaxy formation might violate the standard assumptions. To explore these ideas, we calculate the velocity means, dispersions, covariances, and the anisotropy of the inner halo from observational data using a minimal set of assumptions.

Ideally, our input would be 3-dimensional velocities for a large number of stars covering large areas of sky. Unfortunately, the typical  $\pm 5$  mas yr $^{-1}$  proper motion uncertainty (Monet et al. 2003) of an  $r = 20$  mag,  $d = 12$  kpc F-type star translates into a  $\pm 284$  km s $^{-1}$  uncertainty in tangential velocity. Tangential velocities are consequently uninformative except in large statistical averages, which remain sensitive to systematic error (Fermani & Schönrich 2013). Radial velocities are about

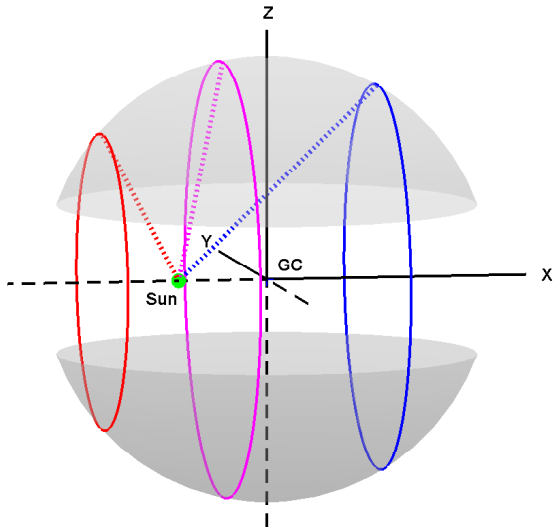


FIG. 5.— Viewing geometry depicting the relation between heliocentric and Galactocentric coordinates systems. Gray spherical caps show  $R = 20$  kpc for  $|Z| > 5$  kpc. Solid circles show where stars with heliocentric distances of  $d = 15$  (red), 20 (purple), and 25 (blue) kpc fall on this  $R = 20$  kpc surface.

25 times more accurate. The typical  $\pm 11 \text{ km s}^{-1}$  radial velocity uncertainty (Lee et al. 2008) for an  $r = 20$  mag star makes radial velocity our tool of choice. Because the Sun lies about 8 kpc from the Galactic center, we use the heliocentric radial velocity, combined with the angular position and the distance of each star, to constrain Galactocentric tangential velocity components.

### 3.1. Projection Factors

Geometrically, the observed line-of-sight velocity,  $v_{los}$ , is the projection of its Galactic velocity components,  $\mathbf{v} = (v_R, v_\theta, v_\phi)$ , on the line-of-sight unit vector,  $\hat{\mathbf{n}}$ ,

$$v_{los} = \mathbf{v} \cdot \hat{\mathbf{n}} = \sum_{i=R,\theta,\phi} v_i p_i, \quad (2)$$

where  $p_i$  are projection factors for each component. We use Galactic spherical coordinates because we are dealing with the halo. The projection factors depend on angular position  $(l, b)$ , heliocentric distance  $d$ , and the distance from the Galactic center  $R$  (see Appendix A.1 for details). Figure 5 illustrates the geometry. Sight lines from the Sun at different Galactic longitude,  $l$ , and latitude,  $b$ , intersect the gray  $R = 20$  kpc surface at points corresponding to different distances from the Sun, although they are all the same distance from the Galactic center.

Importantly, different directions on the sky provide information about different Galactic velocity components. This point is widely understood but rarely quantified. Consider the region on the sky  $|b| > 80^\circ$ : 70% of  $v_{los}$  is in the  $\theta$  component for stars at heliocentric distance  $d = 5$  kpc, but only 20% of  $v_{los}$  is in the  $\theta$  component for stars at  $d = 15$  kpc; the remainder is in the  $R$  component. Recovering tangential velocities from  $v_{los}$  clearly requires large observational samples with broad sky coverage.

Figure 6 quantifies the projection factors from the observer's perspective as functions of angular position  $(l, b)$  and depth. The three columns in Figure 6 are for the  $p_R$ ,  $p_\theta$ , or  $p_\phi$  projection factors. Color indicates the magnitude of the projection factor. The white contours in

each panel mark the regions on the sky at heliocentric distances of  $d = 15, 20$ , and 25 kpc. The three rows in Figure 6 represent Galactocentric distances  $R = 10, 15$ , and 20 kpc. The sky coverage reflects the  $|Z| > 5$  restriction as  $R$  increases.

As expected, information about  $v_\theta$  comes primarily from the Galactic polar regions; information about  $v_\phi$  comes primarily from regions near Galactic latitudes of  $60^\circ$  and  $300^\circ$ . At large distances, the observed line-of-sight velocity contains little information about the tangential velocity components and becomes essentially radial. If there is any correlation between angular position and kinematics, a systematic bias is introduced.

### 3.2. Maximum Likelihood Estimation

We estimate the velocity means, dispersions, covariances, and anisotropy of stars in the halo as functions of distance from the Galactic center using a maximum likelihood procedure. We adopt the standard assumption that the halo star velocities have normal distributions (Binney & Tremaine 2008); see Appendix A.2 for details. This minimal assumption allows us to test whether or not the velocity components are normally distributed, have zero means, and are uncorrelated. Correlations among velocity components, if they exist, may reveal underlying dynamic structures in the halo, such as star streams.

Standard practice is to estimate the velocity dispersions by binning observations in a series of contiguous intervals in  $R$ . This procedure yields a series of discrete estimates, one for each bin. We determine model parameters by maximizing the log likelihood function using analytic first and second derivatives and the R statistical software (R Core Team 2014; Toomet et al. 2012).

We validate our maximum likelihood calculations against a simulated set of stars with  $6 < R < 30$  kpc and normal velocity distributions. Our maximum likelihood calculation finds the correct solution for the underlying model parameters.

We estimate both a restricted and a full statistical model. In the restricted model, the velocities are assumed to have zero means and to be uncorrelated, *i.e.*, the covariance matrix is diagonal, as in previous studies of velocity dispersion in the halo. Estimating the full statistical model allows us to test empirically the assumptions of the restricted model that the velocities have zero means and are uncorrelated and thus test the fundamental assumptions underlying dynamical models of the Milky Way halo. For example, if the gravitational potential is spherically symmetric, the velocity-dispersion tensor is diagonal (Binney & Tremaine 2008).

## 4. RESULTS

We begin by investigating the velocity dispersion and anisotropy of the Milky Way halo using our independent Hectospec F star sample. We then combine our F star sample with the SDSS data sets to test our results with a larger set of observations.

### 4.1. Anisotropy Parameter

One way to characterize the orbital structure of a spherical system, such as the halo, is through the anisotropy parameter defined as (Binney & Tremaine



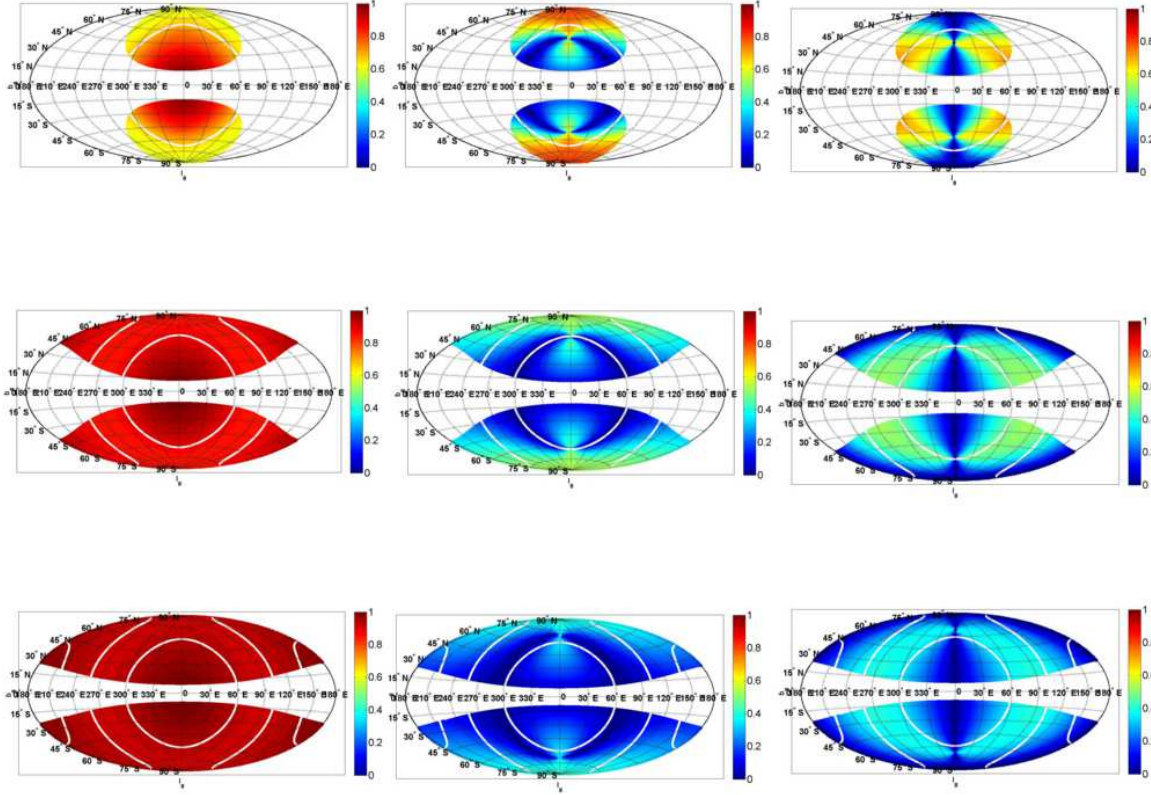


FIG. 6.— Line-of-sight projection factors at different Galactocentric distances in the halo. Columns show the components  $p_R$ ,  $p_\theta$ , and  $p_\phi$ . Rows show the projection factor values at  $R = 10, 15$ , and  $20$  kpc. For reference, white contours mark heliocentric distances of  $d = 15, 20$ , and  $25$  kpc.

2008, eq. 4.61)

$$\beta = 1 - \frac{\sigma_\theta^2 + \sigma_\phi^2}{2\sigma_R^2}. \quad (3)$$

Because the anisotropy parameter depends on the ratio of the velocity dispersions squared, it rapidly becomes more negative as the tangential velocity dispersions increase relative to  $\sigma_R$ . The value of the anisotropy parameter is  $\beta = 1$  for perfectly radial orbits,  $\beta = 0$  for isotropy, and  $\beta = -\infty$  for perfectly circular orbits. From our velocity dispersions estimates, we can quantify the anisotropy of the orbits in the Milky Way halo and investigate the break in  $\beta$  found in previous studies at  $R \simeq 20$  kpc (Kafle et al. 2012; Deason et al. 2013).

#### 4.2. Results from Hectospec F Star Sample

Using the line-of-sight velocities and positions from our Hectospec F star sample, we explore the Galactic radial profile of the velocity dispersions  $\sigma_R$ ,  $\sigma_\theta$ ,  $\sigma_\phi$ , and the anisotropy parameter,  $\beta$ . We begin with the restricted model, which assumes that the velocity components have zero means,  $\mu_i = 0$ , and are uncorrelated,  $\Sigma_{ij} = 0$  for  $i \neq j$ . We relax both of these assumptions when we investigate the larger combined data set in Section 4.3.

To estimate the parameters of our statistical model, we partition our observations into four contiguous radial bins containing  $n_{\text{bin}} = 762$  or  $763$  stars and estimate the parameters and their errors separately for each bin using maximum likelihood. A caret symbol distinguishes our parameter estimates from the parameters themselves. Figure 7 and Appendix A.4 present our estimates of the velocity dispersions and the anisotropy parameter. The

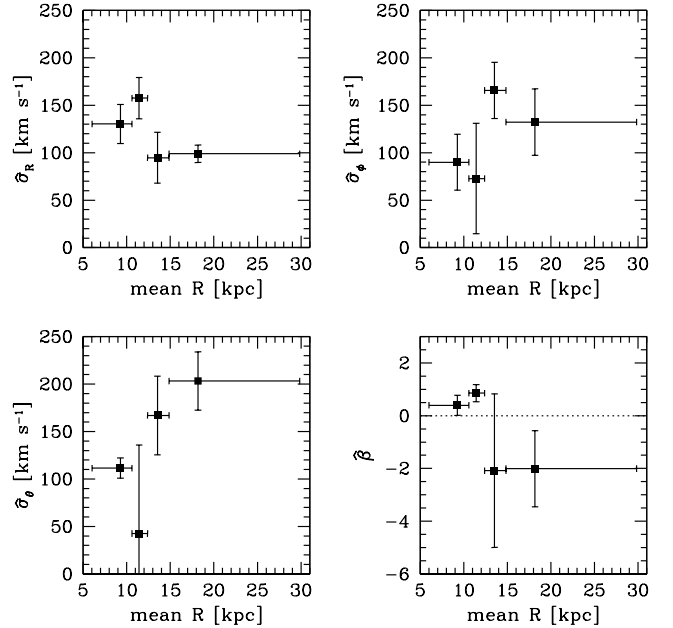


FIG. 7.— Velocity dispersions and anisotropy as function of  $R$  for the Hectospec sample. The 3,049 stars in the Hectospec sample are partitioned into four radial bins of equal numbers. The estimates are plotted at the mean value of  $R$  for stars in each bin. Horizontal error bars show bin size; vertical error bars show  $1\sigma$  uncertainties. Appendix A.4 presents the numbers.

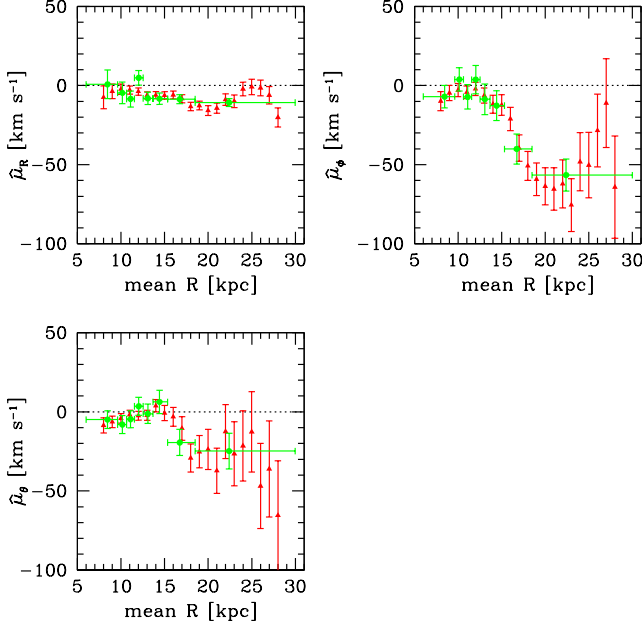


FIG. 8.— Mean velocity components of the combined sample. The 19,859 stars in the combined sample are partitioned into eight radial bins with equal numbers of stars (green circles) and also into overlapping bins of fixed 4 kpc width (red triangles). Horizontal error bars show bin size; vertical error bars show  $1\sigma$  uncertainties. The estimate of  $\bar{v}_\phi$  drops significantly between  $15 \lesssim R \lesssim 25$  kpc.

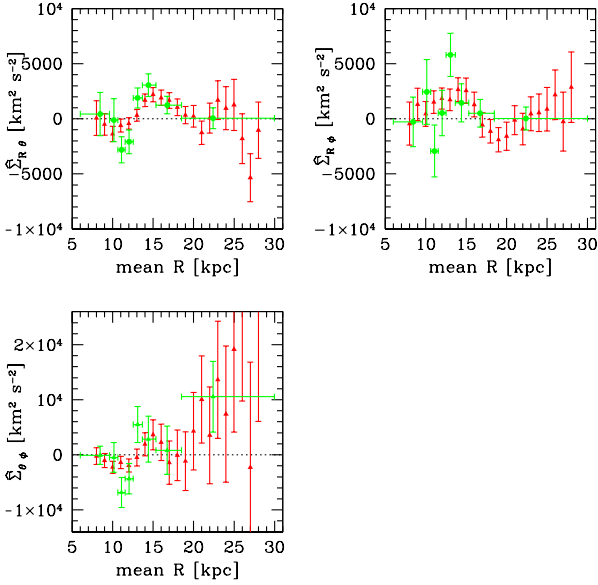


FIG. 9.— Velocity covariances for the combined sample. Sample, error bars, and bins as in Figure 8. Note the significant positive covariance between  $v_R$  and  $v_\theta$  in the region  $R = 14 - 17$  kpc.

solid points in Figure 7 represent the value of the point estimate for the observations in a bin plotted at the mean  $R$  for stars in that bin. The vertical lines mark the  $1\sigma$  confidence intervals for the estimates. Note that the width of the bins varies as a function of Galactic radius,  $R$ , due to the declining number density of stars and the limiting magnitude of the observations. Taken together the graphs reveal how the velocity dispersions and the

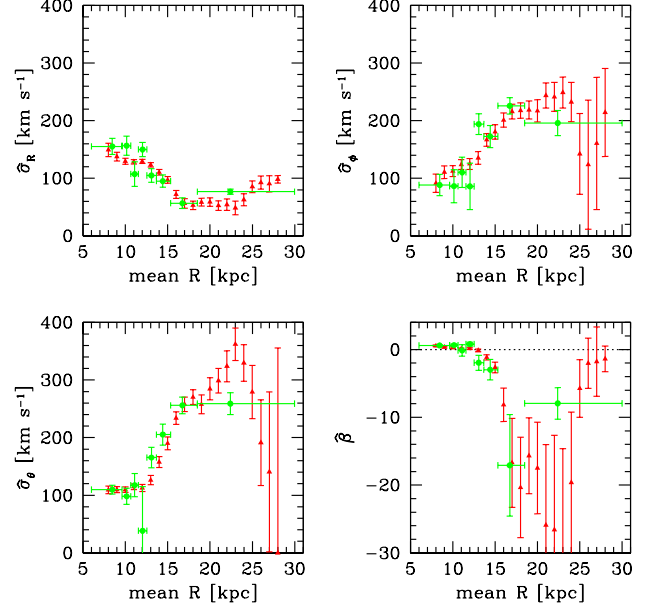


FIG. 10.— Velocity dispersions and anisotropy for the combined sample. Sample, error bars, and bins as in Figure 8. The fixed width bins (red triangles) overlap in  $R$  and have a varying number of stars per bin, whereas the fixed number bins (green circles) have varying widths that do not overlap. Either way, there is a large increase in estimated  $\hat{\sigma}_\theta$  and  $\hat{\sigma}_\phi$ , and a corresponding drop in anisotropy  $\hat{\beta}$ , in the range  $15 \lesssim R \lesssim 25$  kpc.

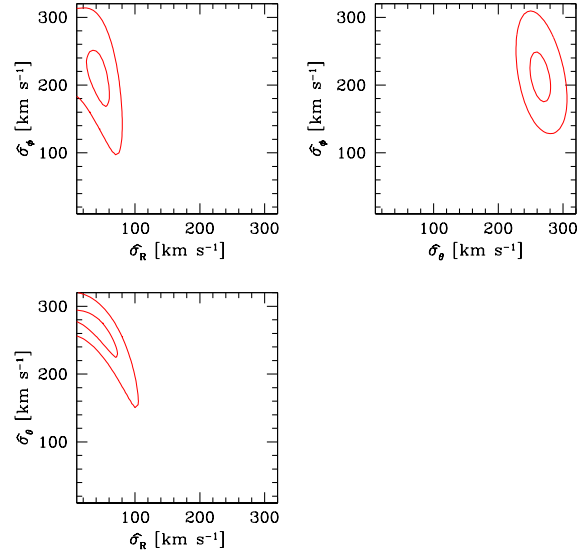


FIG. 11.— Contours of constant  $\chi^2$  illustrating the correlation between the velocity dispersion components in the  $14 < R < 18$  kpc bin. The dispersion  $\hat{\sigma}_\phi$  shows the largest range of values and thus is the most poorly constrained, while  $\hat{\sigma}_R$  and  $\hat{\sigma}_\theta$  are better constrained but correlated.

anisotropy parameter vary with Galactic radius for the F stars in our sample lying more than 5 kpc above the Galactic plane with  $6 < R < 30$  kpc.

The results for  $\hat{\sigma}_R$  and those for the first two points of  $\hat{\sigma}_\theta$ ,  $\hat{\sigma}_\phi$ , and  $\hat{\beta}$  are consistent with previous findings. The drop in the anisotropy parameter occurs near the discontinuity observed previously by others. Large values

for the tangential velocity dispersions  $\hat{\sigma}_\theta$  and  $\hat{\sigma}_\phi$  lead to a negative value for  $\hat{\beta}$  implying that orbits are tangentially biased at these radii.

These apparent anomalies could arise from several sources. The stellar velocities may not be normally distributed, or they may be correlated. The presence of structure or star streams in the inner halo may account for the discrepancies by violating the underlying assumptions of the spatial symmetry and statistical distribution of stellar velocities.

#### 4.3. Results from Combined Sample

Combining the observations of the Hectospec and SDSS samples provides greater statistical power. With the larger number of observations, we can explore a more complete model of the statistical distribution of halo stars. We relax the assumptions of the restricted model and include estimates of the means of the spatial velocities,  $\mu_i$ , to address the possibility of systematic motions, and the off-diagonal elements of the variance-covariance matrix,  $\Sigma_{ij}$ , to allow for correlated velocities.

Figures 8 - 10 and Appendix A.4 present the maximum likelihood estimates of the mean velocities, velocity dispersions, covariances among the velocities, and anisotropy parameter of the stars in the combined sample. The combined sample includes 19,859 stars spanning  $6 < R < 30$  kpc. We estimate the parameters as a function of Galactic radius using two methods for partitioning the data: 1) placing approximately equal numbers of stars ( $n_{\text{bin}} = 2,482$  or  $2,483$ ) within each interval in  $R$  (green circles) and 2) using bins with a fixed width of 4 kpc (red triangles). The error bars represent  $1\sigma$ . The two partition methods yield similar results.

For  $R < 15$  kpc, the estimated mean velocities are small and, given the estimated errors and the uncertainties in the solar motion, are consistent with zero (Figure 8). Within the range  $15 \lesssim R \lesssim 25$  kpc, however,  $\hat{\mu}_\phi$  and  $\hat{\mu}_\theta$  drop significantly below zero. Within  $15 \lesssim R \lesssim 25$  kpc, the stars have mean velocities  $\hat{\mu}_\phi \simeq -50$  to  $-80$  km s $^{-1}$  and  $\hat{\mu}_\theta \simeq -15$  to  $-40$  km s $^{-1}$ .

The estimated off-diagonal covariances among the velocity components (Figure 9) are consistent with zero at the  $2\sigma$  level with some exceptions. Positive covariances  $\Sigma_{R\theta}$  between  $v_R$  and  $v_\theta$  and  $\Sigma_{R\phi}$  between  $v_R$  and  $v_\phi$  occur in the region  $R = 14 - 17$  kpc, for example. The covariance estimates typically are at least an order of magnitude smaller than the variances, except for the covariance  $\hat{\Sigma}_{\theta\phi}$  between  $v_\theta$  and  $v_\phi$  beyond  $R \gtrsim 20$  kpc (Figure 9), which is poorly estimated. The positive correlation between  $v_\theta$  and  $v_\phi$  occurs in approximately the same region where the mean velocity,  $\mu_\phi$ , turns significantly negative, again suggesting the possibility of correlated motions in this region.

The velocity dispersion estimates exhibit unexpected behavior in the range  $15 \lesssim R \lesssim 25$  kpc. Over the entire span of  $6 < R < 30$  kpc, the radial velocity dispersion,  $\hat{\sigma}_R$ , falls from about 150 km s $^{-1}$  to a low of 50 km s $^{-1}$  and then recovers to about 90 km s $^{-1}$ . The changes in the estimates  $\hat{\sigma}_\theta$  and  $\hat{\sigma}_\phi$  are more dramatic. Over the entire span,  $\hat{\sigma}_\theta$  jumps from about 110 km s $^{-1}$  to a maximum of about 360 km s $^{-1}$ ;  $\hat{\sigma}_\phi$  increases from about 110 km s $^{-1}$  to a peak of about 250 km s $^{-1}$ . Similarly, the anisotropy estimate,  $\hat{\beta}$ , declines from 0.5 to around  $-20$ .

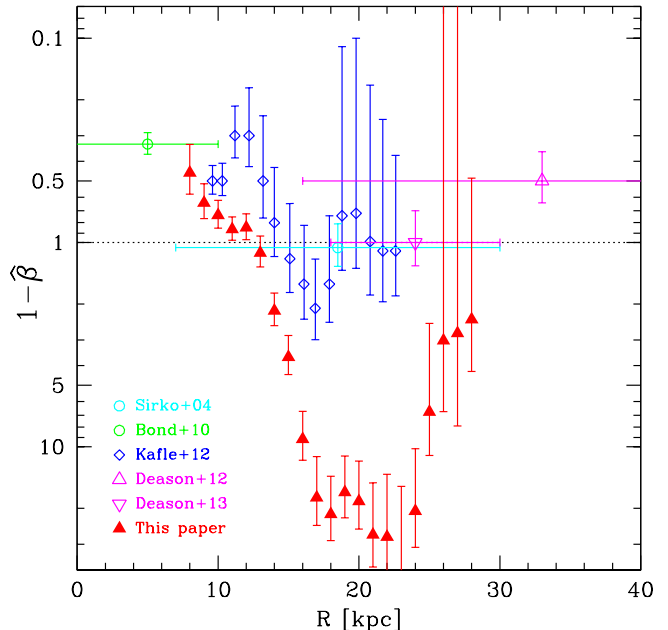


FIG. 12.— Comparison of anisotropy results. We plot the logarithm of  $(1 - \hat{\beta})$  to present a more balanced comparison of tangential and radial anisotropies. We present anisotropy estimates for our overlapping fixed 4 kpc bins (red squares), together with the anisotropy estimates of prior researchers.

To illustrate the correlations among the velocity dispersion components, Figure 11 plots contours of constant  $\chi^2$  for stars in the  $14 < R < 18$  kpc bin. The velocity dispersion estimate  $\hat{\sigma}_\phi$  shows the largest range of values and thus is the most poorly constrained of the three velocity components. The dispersions  $\hat{\sigma}_R$  and  $\hat{\sigma}_\theta$  are better constrained but correlated. Numerically, the maximum likelihood calculation allows the two tangential components to settle around 300 km s $^{-1}$  as  $\hat{\sigma}_R$  goes to zero. This is not a physically plausible scenario. The high velocity dispersions for  $\sigma_\theta$  and  $\sigma_\phi$  and the positive covariance in the range  $14 < R < 18$  kpc imply that some of the stars must have velocities exceeding the Galactic escape velocity.

We compare our results for the anisotropy with previous research in Figure 12. We plot our  $\hat{\beta}$  estimated in fixed width bins of 4 kpc. Our results at  $R < 15$  kpc and at  $R > 25$  kpc are in good agreement with prior research (Sirko et al. 2004; Bond et al. 2010; Kafle et al. 2012; Deason et al. 2012, 2013). In the range  $15 \lesssim R \lesssim 25$  kpc, however, our estimates of  $\beta$  are substantially more negative (corresponding to tangentially biased orbits).

We attribute the less negative values of  $\beta$  estimated by other researchers to their use of much wider bins in  $R$ , which smooth the actual dispersion profiles; to a lower  $Z$  cutoff of 4 kpc, which may increase contamination by disk stars; and to different statistical models that marginalize over tangential velocities and, in some cases, also impose additional assumptions about the gravitational potential and number density of stars. As shown by the horizontal bars in  $R$ , the estimates of  $\beta$  by Sirko et al. (2004), Deason et al. (2012), Kafle et al. (2012), and Deason et al. (2013) are based on broad ranges in  $R$  that extend beyond the interval where our



results diverge. Although Kafle et al. (2012) do not report the sizes of the bins used for their estimations, we deduce from their original data that their bins increase in width from approximately 5 kpc at  $R = 17$  kpc to 7 kpc at  $R = 23$  kpc.

At first glance, our results corroborate the discontinuity in  $\hat{\beta}$  observed around  $R \simeq 20$  kpc. Our results suggest the presence of correlated stellar motions within the region of  $15 \lesssim R \lesssim 25$  kpc, perhaps resulting from star streams or other structure. The implausibly high velocity dispersions also suggest that there may be another explanation for the discrepancy, namely that our underlying statistical model and those of previous researchers may be misspecified. We investigate these possibilities further in Section 5 after first considering the robustness of our results, assessing the alignment of the velocity ellipsoid in the halo, and estimating the mass of the Milky Way interior to  $R = 12$  kpc.

#### 4.4. Robustness of Results

Our results are subject to various sources of potential error. We test the robustness of our parameter estimates with a series of sensitivity analyses on the input data. Systematically overestimating distances, for example, may inflate estimates of the tangential velocities at larger distances causing larger estimates of the tangential velocity dispersions,  $v_\theta$  and  $v_\phi$ , and negatively biasing estimates of the anisotropy  $\beta$ . To investigate the effect of systematic errors in stellar distance estimates, we recompute our results with all distances increased and decreased by 20%. To investigate the effects of our choice of the location of the Sun with respect to the Galactic center, we recompute our results for  $X_\odot = -8.5$  kpc. To investigate our choice of the Sun's circular velocity, we recompute our results for circular velocities of 200 and 250 km s<sup>-1</sup>. To investigate our sensitivity to different parts of the sky, we cut our sample in half in longitude and in latitude.

We also investigate different model specifications, and compare the results from the restricted and unrestricted model for each sample. Finally, the location and size of the bins used in the estimations may affect the results. We therefore re-estimate the model parameters using an Epanechnikov kernel centered at  $R$  with finite support on a total bandwidth of 4 kpc chosen to match the size of fixed bins used. This method gives greater weight to stars near  $R$ , rather than weighting them uniformly as occurs with fixed bins, and provides continuous estimates of the parameters as functions of  $R$ .

In every case, the resulting parameter estimates change by less than about one standard deviation from our original results with the exception of a systematic distance error, where the change in parameter estimates is less than two standard deviations. We conclude that our results are numerically robust within the estimated errors.

#### 4.5. Alignment of the Halo Velocity Ellipsoid and the Gravitational Potential of the Milky Way

The alignment of the velocity ellipsoid for halo stars with respect to the Galactic coordinate system provides a powerful probe of the gravitational potential of the Galaxy. The alignment can be described by the tilt an-

TABLE 1  
TILT ANGLES

$\bar{R}$ (kpc)	$N$	$\alpha_{R\theta}$ (deg)	$\alpha_{R\phi}$ (deg)	$\alpha_{\theta\phi}$ (deg)
16.7	2482	$-2.3^{+2.9}_{-3.6}$	$-1.2^{+5.9}_{-7.3}$	$6.5^{+47.2}_{-55.1}$
22.4	2483	$-0.1^{+2.9}_{-3.6}$	$-0.1^{+5.9}_{-7.3}$	$36.3^{+24.9}_{-55.6}$

gles,  $\alpha_{ij}$ , derived by Smith et al. (2009),

$$\tan(2\alpha_{ij}) = \frac{2\Sigma_{ij}}{\Sigma_{ii} - \Sigma_{jj}}, \quad (4)$$

where  $\Sigma_{ij}$  is the covariance between the velocity components  $v_i$  and  $v_j$ . The tilt angles specify the orientation of the velocity ellipsoid as the angle between the  $i$ -axis and the major axis of the ellipse resulting from the projection of the three dimensional velocity ellipsoid onto the  $ij$ -plane (see, *e.g.*, Binney & Merrifield (1998) and Smith et al. (2009)). Smith et al. (2009) showed that if the inner halo is in steady state and the velocity ellipsoid is everywhere aligned with the Galactic spherical coordinate system, then the gravitational potential must be spherically symmetric. This result holds for the velocity ellipsoid of any tracer population, whether its density distribution is oblate, prolate or triaxial.

We find no evidence of any clear tilt in our analysis of the combined sample using the eight disjoint, approximately equally populated bins of 2,842 or 2,843 stars in the interval  $6 < R < 30$  kpc. None of the estimated tilt angles differs from zero at a  $1\sigma$  statistical significance level. For  $R < 15$  kpc, the tilt angles are poorly estimated: the  $1\sigma$  confidence intervals for the estimates of the tilt angles are of order of tens of degrees. Our most tightly constrained estimates occur for the bins with mean  $\bar{R} = 16.7$  ( $R \in (15.3, 18.5)$ ) kpc and  $\bar{R} = 22.4$  ( $R \in (18.5, 30.0)$ ) kpc. The corresponding estimates for the tilt angles with  $1\sigma$  errors are given in Table 1. None is significantly different from zero even at  $1\sigma$ . The tilt angle  $\alpha_{\theta\phi}$  is less well constrained due primarily to the large uncertainty in estimated covariance between the two components.

Our findings are consistent with a spherically symmetric gravitational potential in the inner halo, as suggested by several recent studies (Smith et al. 2009; Koposov et al. 2010; Agnello & Evans 2012). Our results accord with those of Smith et al. (2009), who found tilt angles consistent with spherical symmetry for  $\sim 1,500$  nearby halo subdwarf stars with heliocentric distances of  $\lesssim 5$  kpc (and  $R \lesssim 11$  kpc) along the  $\sim 250$  deg<sup>2</sup> covered by SDSS Strip 82. Their work was limited both in distance and sky coverage. Our sample, on the other hand, extends to  $R = 30$  kpc with substantially greater sky coverage, including high Galactic latitudes where any contribution from the Galactic disk is negligible.

#### 4.6. Measuring the Interior Mass of the Milky Way

Many studies have exploited the dynamics of halo stars to measure the mass of the Milky Way (Xue et al. 2008; Deason et al. 2012; Kafle et al. 2012) by assuming dynamical equilibrium and fitting specific forms of the distribution function, postulated to depend only on two integrals of motion, the binding energy and the angular

momentum. The mass distribution of the Milky Way is commonly measured using the steady-state Jeans equation for a spherical potential using a tracer population of stars (Binney & Tremaine 2008, eq. 4.37):

$$M(< R) = \frac{R\sigma_R^2}{G} \left( -\frac{d \ln \rho_{tr}}{d \ln R} - \frac{d \ln \sigma_R^2}{d \ln R} - 2\beta \right). \quad (5)$$

The mass interior to a radius  $R$  is a function of the anisotropy,  $\beta$ , and the logarithmic gradients of the radial velocity dispersion,  $\sigma_R$ , and the density of tracers,  $\rho_{tr}$ . The density distribution of stars in the halo has been extensively studied (*e.g.*, Yanny et al. 2000; Chen et al. 2001; Newberg & Yanny 2006; Jurić et al. 2008; Deason et al. 2011) leading to a recent consensus on the density profile (Deason et al. 2011; Sesar et al. 2011) for the inner halo,  $R < 27$  kpc,

$$\rho(R_q) \propto R_q^\alpha, \quad (6)$$

$$R_q^2 = X^2 + Y^2 + \frac{Z^2}{q^2},$$

where the power law index is  $\alpha = -2.3$  to  $-2.6$  and the minor axis to major axis ratio is  $q = 0.6 - 0.7$ . Recent simulations by Wang et al. (2015) evaluate potential biases in estimating the mass of the Milky Way using dynamical tracers. They find that although deviations from spherical symmetry are relatively unimportant, deviations from dynamical equilibrium can cause significant bias. To avoid any discontinuity in the break region, where the assumption of dynamic equilibrium may not hold, we calculate the mass within 12 kpc of the Galactic center,  $M(R \leq 12 \text{ kpc})$ , using the results from the 4 kpc wide bin centered on 12 kpc and the Jeans equation (5). We find  $M(R \leq 12 \text{ kpc}) = 1.3 \times 10^{11} M_\odot$ .

We estimate that the mass uncertainty is 40%, arising largely from the uncertainty in the  $d \ln \sigma_R^2 / d \ln R$  term in Equation 5. The estimated error in  $\sigma_R^2$  is only 10%, and reported values of  $d \ln \rho_{tr} / d \ln R$  also vary by 10%. When we compare adjacent bins to  $R = 12$  kpc to estimate the scatter in  $d \ln \sigma_R^2 / d \ln R$ , however, we find that this term varies by 35%. To compare with previous work, we also calculate the mass for the  $R = 25$  kpc bin. We find  $M(R \leq 25 \text{ kpc}) \simeq 2.6 \times 10^{11} M_\odot$ , a result that agrees to within 20% with Kafle et al. (2012).

## 5. DISCUSSION

Motivated by the large tangential velocity dispersion estimates in the region  $15 \lesssim R \lesssim 25$  kpc, we examine whether the observational data are consistent with our one fundamental assumption: that the three components of velocity,  $(v_R, v_\Theta, v_\Phi)$ , are normally distributed. The normal distribution is described by two parameters, its mean and dispersion. If the distribution of halo star velocities is not intrinsically normal and we (incorrectly) try to represent it as such, we expect the mean will remain largely unchanged but the dispersion will vary. Notably, the Sgr stream passes through our survey region in a way that introduces a bimodal velocity distribution of stars into the sample beginning at  $R \sim 15$  kpc.

### 5.1. Departures from Normality

If the underlying theoretical assumptions are correct, the observed line-of-sight velocities should be normally

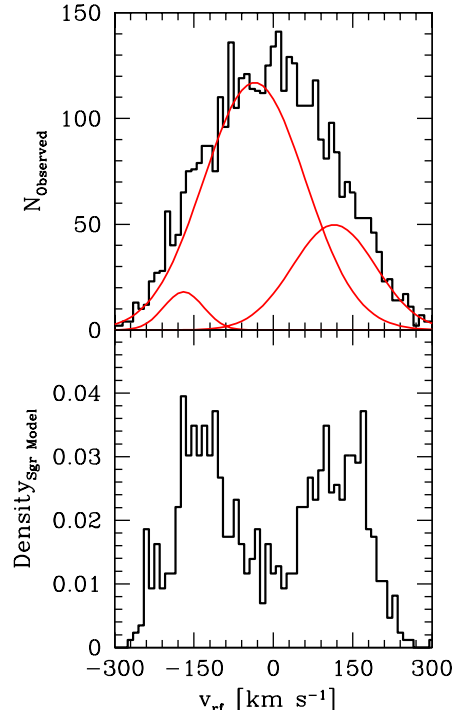


FIG. 13.— Top panel: Observed  $v_{rf}$  distribution of stars in the bin  $14 < R < 18$  kpc, superimposed with a fitted, three-component, normal mixture model (Benaglia et al. 2009). There appears to be an excess of stars in both the negative and positive velocity wings of the distribution. Bottom panel: Distribution of the Law & Majewski (2010) Sgr  $N$ -body model sampled in the identical way for  $14 < R < 18$  kpc. The simulated Sgr stars have a bi-modal distribution of line-of-sight velocities in this region.

distributed since linear combinations of normally distributed random variables are also normally distributed. Yet Section 2.4 shows that the distribution of observed radial velocities departs from normal in certain regions and fails standard statistical tests for normality. Physically, known or unknown star streams or other velocity structure may be responsible for this observed departure from normality. Correlations between angular position and velocity break our model assumptions.

To better understand the possible causes of these discrepancies, we look more closely at the break region by selecting the 4,077 stars in the  $14 < R < 18$  kpc bin and plotting the histogram of  $v_{rf}$  in Figure 13. The histogram reveals deviations from a normal distribution both in the center and in the wings of the distribution. The Kolmogorov-Smirnov test rejects normality at a reasonable level of statistical significance ( $p = 0.069$ ), and the more powerful Anderson-Darling test that gives more weight to the tails than the Kolmogorov-Smirnov test strongly rejects normality ( $p = 9.9 \times 10^{-8}$ ).

### 5.2. Non-Normality of Sgr Stream Velocities

At least one significant halo structure lies within our survey footprint: the Sgr stream. To assess the impact of the Sgr stream, we turn to the  $N$ -body model of Law & Majewski (2010). Their model is designed to match existing observational constraints on the location and motion of the Sgr stream in a triaxial potential. We sample the  $N$ -body model for test particles that lie at  $|Z| > 5$  kpc in the range  $14 < R < 18$  kpc and that

fall within an approximation of our survey footprint on the sky ( $b \geq 30^\circ$  or ( $b \leq -30^\circ$  and  $l \in (50^\circ, 200^\circ)$ )). Although the majority of Sgr is at larger distances, a fraction of the stream is present in the  $14 < R < 18$  kpc region. Figure 13 (lower panel) shows the  $v_{rf}$  distribution of Sgr  $N$ -body particles in this region.

Because the Sgr stream wraps around the sky in a roughly polar orbit, the Sgr stars passing through the  $14 < R < 18$  kpc region exhibit multiple velocity peaks and a broad velocity dispersion. Suggestively, the two main peaks in  $v_{rf}$  from the Sgr model coincide with the excesses found in the wings of the observed halo star distribution (Figure 13) in a fitted, three component, normal mixture model (Benaglia et al. 2009).

Previous research estimates that up to 10% of the stars in the survey region may originate in the Sgr stream (King et al. 2012). The presence of Sgr stream stars in our sample may thus account, at least partially, for the observed discrepancies in the observed velocity dispersions and anisotropy of the halo in the break region. We test this hypothesis by removing all stars in our sample within  $10^\circ$  of the Sgr stream,  $|B| < 10^\circ$ , using the Sgr stream coordinates,  $(\Lambda, B)$ , defined by Belokurov et al. (2014).

Removing the region of the Sgr stream from our sample modestly lowers our estimates of the dispersions, which, in turn, increases our estimate of the anisotropy. The anisotropy in the  $14 < R < 18$  kpc bin changes from  $\beta = -8$  to  $\beta = -6$ , in better agreement with previous results (Figure 12). The change in  $\beta$  is formally less than  $1\sigma$ , but there may be other star streams for which we do not account. Indeed, Bell et al. (2008) and Schlafman et al. (2009) identify 30% - 40% of F-type stars at 15 kpc depths in coherent spatial or velocity structures, and Janesh et al. (2015) show that the percentage of halo stars in coherent structures increases with depth. We conclude that the traditionally assumed normal velocity distribution model may not properly represent the substructure of the stellar halo.

## 6. CONCLUSION

We use a large sample of 19,859 stars at  $6 < R < 30$  kpc to investigate the mean velocities, velocity dispersions, covariances, and anisotropy of the Milky Way halo. This dense sample enables finer binning than previously used and allows us to investigate the  $15 \lesssim R \lesssim 25$  kpc anomaly in anisotropy at higher statistical significance.

We begin by presenting a new radial velocity survey of 6,174 faint F-type stars observed with the Hectospec spectrograph using the MMT telescope. F-type stars are dense tracers of both the thick disk and halo. To focus on halo kinematics, we restrict our analysis to stars with  $|Z| > 5$  kpc. We add stars from published SDSS radial velocity samples to create a combined sample of 19,859 stars that span  $6 < R < 30$  kpc.

We use the Sun's offset from the Galactic center to recover tangential velocity information from the observed line-of-sight velocities utilizing standard statistical methods. We make the minimal assumption that the underlying stellar velocity distribution is normal. We use a maximum likelihood procedure to calculate the velocity means, dispersions, covariances, and anisotropy. We find that the alignment of the velocity ellipsoid is consistent with a spherically symmetric gravitational potential.

From the spherical Jeans equation, we estimate the mass of the Milky Way within 12 kpc is  $M(R \leq 12 \text{ kpc}) = 1.3 \times 10^{11} M_\odot$  with an uncertainty of 40%.

A significant region of discontinuity  $15 \lesssim R \lesssim 25$  kpc exists where the estimated velocity dispersions and anisotropy diverge from their anticipated values, confirming the break region observed by others. The estimated tangential velocity dispersions in this region are so large that stars would be unbound, an unphysical result. Yet the results are numerically robust. In sensitivity analyses (*i.e.*, using a different solar motion, different distance scale, different survey footprint, etc.), the maximum likelihood calculation yields parameters that change by less than about one standard deviation from our original result. Conversely, if we input simulated data drawn from known normal velocity distributions, the maximum likelihood estimation finds the correct velocity dispersion and anisotropy parameters.

We suggest that the discontinuity in the region  $15 \lesssim R \lesssim 25$  kpc arises from the failure of the normal distribution model to describe the actual velocity data. Physically, known or unknown star streams or other velocity substructure may be responsible for the departure from normality. The predicted contribution of the (polar orbiting) Sgr stream in our survey region, for example, is a bi-modal distribution of stars in the wings of the observed radial velocity distribution. Sgr by itself cannot explain the discontinuity, but Sgr is unlikely to be the only structure in the halo.

The upshot is that larger radial velocity samples alone cannot improve our understanding of the halo using the standard statistical approach. Significant improvement requires direct tangential velocity constraints for halo stars, like those soon to be provided by *Gaia*. The combination of our radial velocity measurements with *Gaia* proper motions will thus be very useful for understanding the physical nature of the  $15 \lesssim R \lesssim 25$  kpc discontinuity region and the kinematics of the Milky Way halo.

We thank Mike Alegria, Perry Berlind, Mike Calkins, Nelson Caldwell, Scott Gotilla, John McAfee, Erin Martin, and Ale Milone for their assistance with observations obtained at the MMT Observatory, a joint facility of the Smithsonian Institution and the University of Arizona. We also thank William B. Simpson for helpful comments, Alis J. Deason for kindly providing data for Figure 12, and David R. Law for kindly providing the Sgr  $N$ -body model. CK dedicates this work to Carlos A. Berenstein. This paper uses data products created by the OIR Telescope Data Center, supported by the Smithsonian Astrophysical Observatory, and data products from the Sloan Digital Sky Survey, which is managed by the Astrophysical Research Consortium for the Participating Institutions. This research also makes use of NASA's Astrophysics Data System Bibliographic Services. This work was supported by the Smithsonian Institution. CK gratefully acknowledges additional support from the Pleiades Consulting Group, Inc.

*Facilities:* MMT (Hectospec spectrograph)

## REFERENCES

- Abadi, M. G., Navarro, J. F., & Steinmetz, M. 2006, *MNRAS*, 365, 747
- Agnello, A. & Evans, N. W. 2012, *MNRAS*, 422, 1767
- Allende Prieto, C., Fernández-Alvar, E., Schlesinger, K. J., et al. 2014, *A&A*, 568, A7
- Allende Prieto, C., Sivarani, T., Beers, T. C., et al. 2008, *AJ*, 136, 2070
- Beers, T. C., Carollo, D., Ivezić, Ž., et al. 2012, *ApJ*, 746, 34
- Bell, E. F., Zucker, D. B., Belokurov, V., et al. 2008, *ApJ*, 680, 295
- Belokurov, V., Koposov, S. E., Evans, N. W., et al. 2014, *MNRAS*, 437, 116
- Benaglia, T., Chauveau, D., Hunter, D. R., & Young, D. 2009, *Journal of Statistical Software*, 32, 1
- Binney, J. & Merrifield, M. 1998, *Galactic Astronomy* (Princeton University Press)
- Binney, J. & Tremaine, S. 2008, *Galactic Dynamics: Second Edition* (Princeton University Press)
- Bond, N. A., Ivezić, Ž., Sesar, B., et al. 2010, *ApJ*, 716, 1
- Bovy, J., Allende Prieto, C., Beers, T. C., et al. 2012, *ApJ*, 759, 131
- Bressan, A., Marigo, P., Girardi, L., et al. 2012, *MNRAS*, 427, 127
- Brown, W. R., Allende Prieto, C., Beers, T. C., et al. 2003, *AJ*, 126, 1362
- Brown, W. R., Beers, T. C., Wilhelm, R., et al. 2008, *AJ*, 135, 564
- Brown, W. R., Geller, M. J., Kenyon, S. J., & Diaferio, A. 2010, *AJ*, 139, 59
- Brown, W. R., Geller, M. J., Kenyon, S. J., & Kurtz, M. J. 2005a, *ApJ*, 622, L33
- Brown, W. R., Geller, M. J., Kenyon, S. J., et al. 2005b, *AJ*, 130, 1097
- Bullock, J. S. & Johnston, K. V. 2005, *ApJ*, 635, 931
- Carollo, D., Beers, T. C., Chiba, M., et al. 2010, *ApJ*, 712, 692
- Carollo, D., Beers, T. C., Lee, Y. S., et al. 2007, *Nature*, 450, 1020
- Chen, B., Stoughton, C., Smith, J. A., et al. 2001, *ApJ*, 553, 184
- Deason, A. J., Belokurov, V., & Evans, N. W. 2011, *MNRAS*, 416, 2903
- Deason, A. J., Belokurov, V., Evans, N. W., & An, J. 2012, *MNRAS*, 424, L44
- Deason, A. J., Van der Marel, R. P., Guhathakurta, P., Sohn, S. T., & Brown, T. M. 2013, *ApJ*, 766, 24
- Fabricant, D., Fata, R., Roll, J., et al. 2005, *PASP*, 117, 1411
- Fermani, F. & Schönrich, R. 2013, *MNRAS*, 432, 2402
- Font, A. S., McCarthy, I. G., Crain, R. A., et al. 2011, *MNRAS*, 416, 2802
- Girardi, L., Bertelli, G., Bressan, A., et al. 2002, *A&A*, 391, 195
- Ibata, R. A., Gilmore, G., & Irwin, M. J. 1994, *Nature*, 370, 194
- Ivezić, Ž. et al. 2008, *ApJ*, 684, 287
- Janesh, W., Morrison, H. L., Ma, Z., et al. 2015, *ApJ*, submitted
- Jeans, J. H. 1915, *MNRAS*, 76, 70
- Johnston, K. V., Bullock, J. S., Sharma, S., et al. 2008, *ApJ*, 689, 936
- Jurić, M. et al. 2008, *ApJ*, 673, 864
- Kaffe, P. R., Sharma, S., Lewis, G. F., & Bland-Hawthorn, J. 2012, *ApJ*, 761, 98
- . 2014, *ApJ*, 794, 59
- King, III, C., Brown, W. R., Geller, M. J., & Kenyon, S. J. 2012, *ApJ*, 750, 81
- Koposov, S. E., Rix, H.-W., & Hogg, D. W. 2010, *ApJ*, 712, 260
- Kurtz, M. J. & Mink, D. J. 1998, *PASP*, 110, 934
- Law, D. R. & Majewski, S. R. 2010, *ApJ*, 714, 229
- Lee, Y. S., Beers, T. C., Sivarani, T., et al. 2008, *AJ*, 136, 2022
- Loebman, S. R., Ivezić, Ž., Quinn, T. R., et al. 2014, *ApJ*, 794, 151
- Majewski, S. R., Skrutskie, M. F., Weinberg, M. D., & Ostheimer, J. C. 2003, *ApJ*, 599, 1082
- Marigo, P., Girardi, L., Bressan, A., et al. 2008, *A&A*, 482, 883
- McCarthy, I. G., Font, A. S., Crain, R. A., et al. 2012, *MNRAS*, 420, 2245
- McMillan, P. J. & Binney, J. J. 2010, *MNRAS*, 402, 934
- Mink, D. J., Wyatt, W. F., Caldwell, N., et al. 2007, in *Astronomical Society of the Pacific Conference Series*, Vol. 376, *Astronomical Data Analysis Software and Systems XVI*, ed. R. A. Shaw, F. Hill, & D. J. Bell, 249
- Monet, D. G., Levine, S. E., Canzian, B., et al. 2003, *AJ*, 125, 984
- Newberg, H. J. & Yanny, B. 2006, *Journal of Physics Conference Series*, 47, 195
- Newby, M., Newberg, H. J., Simones, J., Cole, N., & Monaco, M. 2011, *ApJ*, 743, 187
- R Core Team. 2014, *R: A Language and Environment for Statistical Computing*, R Foundation for Statistical Computing, Vienna, Austria
- Rashkov, V., Pillepich, A., Deason, A. J., et al. 2013, *ApJ*, 773, L32
- Reed, B. C. 2006, *JRASC*, 100, 146
- Reid, M. J., Menten, K. M., Brunthaler, A., et al. 2014, *ApJ*, 783, 130
- Reid, M. J., Menten, K. M., Zheng, X. W., et al. 2009, *ApJ*, 700, 137
- Schlafman, K. C., Rockosi, C. M., Allende Prieto, C., et al. 2009, *ApJ*, 703, 2177
- Schlegel, D. J., Finkbeiner, D. P., & Davis, M. 1998, *ApJ*, 500, 525
- Schönrich, R., Asplund, M., & Casagrande, L. 2011, *MNRAS*, 415, 3807
- . 2014, *ApJ*, 786, 7
- Schönrich, R., Binney, J., & Dehnen, W. 2010, *MNRAS*, 403, 1829
- Schwarzschild, K. 1907, *Nachrichten von der Gesellschaft der Wissenschaften zu Göttingen, Mathematisch-Physikalische Klasse*, 1907, 614
- Searle, L. & Zinn, R. 1978, *ApJ*, 225, 357
- Sesar, B., Ivezić, Ž., Stuart, J. S., et al. 2013, *AJ*, 146, 21
- Sesar, B., Jurić, M., & Ivezić, Ž. 2011, *ApJ*, 731, 4
- Sirko, E., Goodman, J., Knapp, G. R., et al. 2004, *AJ*, 127, 914
- Smith, M. C., Wyn Evans, N., & An, J. H. 2009, *ApJ*, 698, 1110
- Toomet, O., Henningsen, A., & with contributions from Graves, S. and Croissant, Y. 2012, *maxLik: Maximum Likelihood Estimation*, R package version 1.1-2
- Wang, W., Han, J., Cooper, A., et al. 2015, *MNRAS*, 453, 377
- Watkins, L. L., Evans, N. W., Belokurov, V., et al. 2009, *MNRAS*, 398, 1757
- Xue, X.-X., Rix, H.-W., Yanny, B., et al. 2011, *ApJ*, 738, 79
- Xue, X. X., Rix, H. W., Zhao, G., et al. 2008, *ApJ*, 684, 1143
- Yanny, B., Newberg, H. J., Kent, S., et al. 2000, *ApJ*, 540, 825
- Zolotov, A., Willman, B., Brooks, A. M., et al. 2009, *ApJ*, 702, 1058

## APPENDIX

## APPENDIX

*Coordinate Systems and Projection Factors*

We employ four coordinates systems: heliocentric Cartesian  $(x, y, z)$  and spherical  $(d, b, l)$  coordinates, and Galactocentric Cartesian  $(X, Y, Z)$  and spherical  $(R, \theta, \phi)$  coordinates. In the Cartesian coordinate systems, the Galactocentric  $X$ - and  $Y$ -axes lie in the Galactic plane; the heliocentric  $xy$ -plane is parallel to, but slightly above, the Galactic plane since the Sun lies slightly above it. The  $z$ - and  $Z$ -axes are perpendicular to the  $xy$ - and  $XY$ -planes, respectively, forming right-handed coordinate systems. The positive  $x$ - and  $X$ -directions are defined as from the Sun toward the Galactic center. Since the Sun is located 8 kpc from the Galactic center and 0.0196 kpc above the Galactic plane (Reed 2006), the two Cartesian coordinate systems transform as

$$X = x - 8.0, \quad Y = y, \quad Z = z + 0.0196 \text{ kpc} \quad (\text{A1})$$

The spherical coordinates are defined in terms of their Cartesian coordinates with radii  $d = \sqrt{x^2 + y^2 + z^2}$  and  $R = \sqrt{X^2 + Y^2 + Z^2}$  for the heliocentric and Galactocentric systems, respectively. Longitudes  $l$  and  $\phi$  are measured in the  $xy$ - or  $XY$ - plane from the  $x$ - or  $X$ -axis toward the  $y$ - or  $Y$ -axis. The second angle of the spherical coordinates is defined differently for the heliocentric and Galactocentric systems. For the heliocentric system,  $b$  is defined as the latitude, the angle measured from the  $xy$ -plane with the direction toward the  $z$ -axis taken as positive. For the Galactocentric system,  $\theta$  is defined as the colatitude, the angle measured from the  $Z$ -axis.

The line-of-sight velocity component projection factors are:

$$p_R = \cos b \cos l \sin \theta \cos \phi + \cos b \sin l \sin \theta \sin \phi + \sin b \cos \theta \quad (\text{A2})$$

$$p_\theta = \cos b \cos l \cos \theta \cos \phi + \cos b \sin l \cos \theta \sin \phi - \sin b \sin \theta \quad (\text{A3})$$

$$p_\phi = -\cos b \cos l \sin \phi + \cos b \sin l \cos \phi \quad (\text{A4})$$

A projection factor  $p_\theta = 0.3$ , for example, means that a tangential velocity component of  $v_\theta = 100 \text{ km s}^{-1}$  contributes  $30 \text{ km s}^{-1}$  to the line-of-sight velocity,  $v_{los}$ .

*Probability Density Function*

Following standard theoretical development, we assume that the components of stellar velocity,  $v_i$ , are normally distributed with means,  $\mu_i$ , and standard deviations,  $\sigma_i$ ,

$$v_i \sim N(\mu_i, \sigma_i^2), \quad i \in \{R, \theta, \phi\}. \quad (\text{A5})$$

The observed line-of-sight velocity for a given star is then the sum of the projections of each velocity component onto the line of sight, as previously defined in Equation 2. Because the line-of-sight velocity is a linear combination of the velocity components, assumed to be normally distributed, the observed line-of-sight velocity is also normally distributed with mean,

$$E[v_{los}] = p_R \mu_R + p_\theta \mu_\theta + p_\phi \mu_\phi = \mathbf{p}' \boldsymbol{\mu}, \quad (\text{A6})$$

and variance,

$$\text{Var}[v_{los}] = \text{Var}[\mathbf{p}' \mathbf{v}] = \mathbf{p}' \boldsymbol{\Sigma} \mathbf{p}, \quad (\text{A7})$$

where  $\boldsymbol{\Sigma} = [\Sigma_{ij}]$  is the variance-covariance matrix among the  $v_i$  and is symmetric,  $\Sigma_{ij} = \Sigma_{ji}$ . Combining these results yields the distribution of line-of-sight velocities

$$\begin{aligned} v_{los} &\sim N(\mathbf{p}' \boldsymbol{\mu}, \mathbf{p}' \boldsymbol{\Sigma} \mathbf{p}) \\ &= N(p_R \mu_R + p_\theta \mu_\theta + p_\phi \mu_\phi, \\ &\quad p_R^2 \Sigma_{RR} + p_\theta^2 \Sigma_{\theta\theta} + p_\phi^2 \Sigma_{\phi\phi} + 2p_R p_\theta \Sigma_{R\theta} + 2p_R p_\phi \Sigma_{R\phi} + 2p_\theta p_\phi \Sigma_{\theta\phi}) \end{aligned} \quad (\text{A8})$$

Now consider the probability  $f(x|\boldsymbol{\Theta})$  for finding a star at Galactic coordinates  $(R, \theta, \phi)$  with line-of-sight velocity  $v_{los}$ . Defining an observation as  $x = \{R, \theta, \phi, v_{los}\}$  and the model parameters as  $\boldsymbol{\Theta} = \{\boldsymbol{\mu}, \boldsymbol{\Sigma}\}$ , the probability distribution function is

$$f(x|\boldsymbol{\Theta}) = \frac{\rho(\vec{R})}{\sqrt{2\pi} \sqrt{\mathbf{p}' \boldsymbol{\Sigma} \mathbf{p}}} \exp \left[ -\frac{1}{2} \frac{(v_{los} - \mathbf{p}' \boldsymbol{\mu})^2}{\mathbf{p}' \boldsymbol{\Sigma} \mathbf{p}} \right] \propto \frac{1}{\sqrt{\mathbf{p}' \boldsymbol{\Sigma} \mathbf{p}}} \exp \left[ -\frac{1}{2} \frac{(v_{los} - \mathbf{p}' \boldsymbol{\mu})^2}{\mathbf{p}' \boldsymbol{\Sigma} \mathbf{p}} \right], \quad (\text{A9})$$

where  $\rho(\vec{R})$  is the number density of stars. This generalization of the Schwarzschild distribution, originally proposed by Schwarzschild (1907) to model the velocity distribution of stars in the solar neighborhood, further allows correlations among the spatial velocities. Since  $\rho(\vec{R})$  is not a function of the model parameters, it may be omitted as it does



TABLE 2  
HECTOSPEC F STARS

R.A. (h:m:s)	Decl. (d:m:s)	$v_{\text{helio}}$ (km s <sup>-1</sup> )	$r_0$ (mag)	$M_r$ (mag)	$R$ (kpc)	$Z$ (kpc)
0:39:30.452	+25:14:52.60	$-287.6 \pm 19.8$	$19.940 \pm 0.027$	5.241	13.94	-5.31
0:39:59.518	+25:12:41.95	$-44.8 \pm 18.7$	$20.182 \pm 0.028$	5.821	12.89	-4.54
0:41:30.298	+25:09:09.98	$-167.8 \pm 26.6$	$20.520 \pm 0.043$	6.412	12.25	-4.05
0:41:43.272	+25:55:22.42	$-224.6 \pm 12.4$	$19.196 \pm 0.018$	4.790	13.07	-4.57
0:41:44.054	+25:01:11.58	$-75.9 \pm 23.3$	$20.510 \pm 0.037$	5.247	16.22	-6.92

NOTE. — (This table is available in its entirety in machine-readable and Virtual Observatory forms in the online journal. A portion is shown here for guidance regarding its form and content.)

not enter into the subsequent maximum likelihood analysis, an advantage of the maximum likelihood technique. We estimate nine parameters of  $\Theta$  in our statistical model: three means  $\mu_i$  and six independent elements of the symmetric covariance matrix  $\Sigma$ .

Denoting an individual observation by  $x = \{R, \theta, \phi, v_{los}\}$  and a set of observations by  $\mathbf{x} = \{x_1, x_2 \dots x_n\}$ , the log likelihood function is

$$\mathcal{L}(\Theta|\mathbf{x}) = \sum_{i=1}^n \log f(x_i|\Theta). \quad (\text{A10})$$

#### Data Table

Table 2 presents the clean sample of 6,174 F-type stars from the Hectospec radial velocity survey. For each star we list the position (epoch J2000), our heliocentric radial velocity measurement, the SDSS DR10 de-reddened  $r$ -band magnitude, our estimated absolute magnitude  $M_r$  using the Ivezić et al. (2008) photometric parallax relation, and the corresponding Galactocentric radial  $R$  and vertical  $Z$  distances, calculated assuming the Sun is at  $R = 8$  kpc. The full version of Table 2 is available in the online journal.

#### Results Table

Table 3 presents the estimation results for the Hectospec F star and combined samples.

TABLE 3  
ESTIMATION RESULTS

$N$	$R_{min}$ (kpc)	$R_{max}$ (kpc)	$\bar{R}$ (kpc)	$\mu_R$ (km s <sup>-1</sup> )	$\mu_\theta$ (km s <sup>-1</sup> )	$\mu_\phi$ (km s <sup>-1</sup> )	$\sigma_R$ (km s <sup>-1</sup> )	$\sigma_\theta$ (km s <sup>-1</sup> )	$\sigma_\phi$ (km s <sup>-1</sup> )	$\Sigma_{R\theta}$ (km <sup>2</sup> s <sup>-2</sup> )	$\Sigma_{R\phi}$ (km <sup>2</sup> s <sup>-2</sup> )	$\Sigma_{\theta\phi}$ (km <sup>2</sup> s <sup>-2</sup> )	$\beta$
Hectospec F Star Sample													
762	6.0	10.6	9.3				130.3 (20.6)	111.5 (10.7)	90.0 (29.5)				0.40 (0.38)
762	10.6	12.4	11.4				157.5 (21.6)	42.5 (93.2)	72.8 (58.2)				0.86 (0.33)
762	12.4	14.9	13.5				94.7 (26.7)	167.0 (41.4)	165.6 (29.6)				-2.08 (2.91)
763	14.9	29.8	18.2				98.9 (9.2)	203.3 (30.7)	132.3 (35.0)				-2.01 (1.44)
Combined Sample - equally populated bins													
2483	6.0	9.6	8.4	0.8 (9.1)	-4.9 (5.6)	-7.0 (7.1)	155.3 (14.0)	109.8 (7.8)	88.3 (18.6)	428.7 (1971.1)	-271.8 (2251.1)	-80.4 (1670.5)	0.59 (0.13)
2482	9.6	10.6	10.1	-4.6 (6.9)	-8.0 (5.7)	3.9 (7.4)	156.5 (16.5)	98.2 (14.2)	86.2 (28.7)	-123.2 (1949.6)	2442.2 (2944.3)	-456.0 (2712.9)	0.65 (0.19)
2482	10.6	11.5	11.1	-8.5 (5.1)	-4.7 (5.4)	-7.2 (7.7)	107.4 (21.5)	117.6 (20.3)	110.3 (26.3)	-2806.8 (1190.2)	-2923.5 (2357.3)	-6839.6 (2723.3)	-0.13 (0.83)
2482	11.5	12.5	12.0	4.9 (4.6)	3.5 (5.7)	3.8 (9.0)	150.1 (12.3)	38.5 (76.6)	85.9 (40.2)	-2088.1 (1071.4)	530.2 (2054.6)	-4335.6 (2761.1)	0.80 (0.29)
2483	12.5	13.7	13.1	-8.1 (3.9)	-1.2 (6.1)	-8.6 (9.7)	105.0 (11.8)	165.4 (17.8)	194.0 (17.9)	1896.4 (913.9)	5801.2 (1961.8)	5498.6 (3269.4)	-1.95 (1.11)
2482	13.7	15.3	14.4	-8.3 (3.6)	6.3 (7.3)	-12.7 (9.4)	95.1 (10.6)	205.3 (18.3)	172.6 (19.2)	3053.6 (1023.6)	1448.5 (1732.2)	2843.3 (4172.5)	-2.97 (1.52)
2482	15.3	18.5	16.7	-8.6 (2.9)	-19.4 (8.3)	-40.1 (9.5)	56.8 (9.3)	256.0 (14.4)	225.8 (14.2)	1243.5 (793.6)	494.8 (1257.0)	831.7 (4391.9)	-17.08 (7.50)
2483	18.5	30.0	22.4	-10.7 (2.4)	-24.8 (11.3)	-56.6 (10.1)	76.8 (4.7)	259.1 (18.8)	195.8 (21.7)	57.2 (952.3)	30.9 (1046.3)	10559.0 (6406.6)	-7.95 (2.32)
Combined Sample - 4 kpc bins													
3356	6	10	8.8	-7.4 (7.3)	-8.6 (4.8)	-9.9 (6.1)	149.4 (11.6)	109.4 (6.6)	91.5 (15.8)	65.0 (1566.3)	-438.2 (1951.8)	-212.8 (1512.3)	0.54 (0.12)
5680	7	11	9.7	-3.6 (4.6)	-6.3 (3.6)	-4.7 (4.7)	137.7 (7.5)	109.8 (5.3)	110.5 (11.0)	-505.9 (987.4)	1309.8 (1460.6)	-1025.6 (1263.4)	0.36 (0.12)
7915	8	12	10.4	-2.3 (3.3)	-4.1 (3.0)	-2.9 (4.2)	129.6 (5.2)	109.9 (4.8)	112.6 (9.4)	-1373.8 (692.5)	447.5 (1124.0)	-2247.6 (1088.7)	0.26 (0.11)
9505	9	13	11.1	-2.8 (2.7)	-1.8 (2.8)	-4.2 (4.0)	128.6 (3.9)	114.8 (4.9)	123.9 (8.6)	-603.9 (594.3)	1515.5 (1023.9)	-1374.5 (1112.6)	0.14 (0.11)
9658	10	14	11.9	-3.8 (2.3)	-2.4 (2.8)	-2.1 (4.2)	129.3 (3.5)	112.7 (6.2)	125.0 (9.5)	-426.5 (518.2)	1837.7 (955.3)	-1941.9 (1186.2)	0.15 (0.12)
8606	11	15	12.8	-6.2 (2.2)	-2.2 (3.2)	-6.3 (4.8)	123.5 (3.9)	126.3 (8.2)	135.3 (11.0)	315.9 (533.1)	1725.8 (989.9)	-471.1 (1543.6)	-0.12 (0.19)
6933	12	16	13.7	-6.1 (2.2)	3.8 (3.9)	-11.8 (5.6)	110.4 (4.8)	157.7 (9.6)	166.7 (11.0)	1687.6 (578.4)	2648.4 (1082.8)	1922.0 (2092.4)	-1.16 (0.39)
5354	13	17	14.6	-6.2 (2.3)	-0.7 (4.8)	-12.3 (6.5)	97.2 (5.8)	190.1 (11.1)	180.4 (12.4)	2195.8 (641.7)	2557.4 (1142.6)	3649.3 (2718.3)	-2.64 (0.79)
4077	14	18	15.6	-5.9 (2.4)	-3.1 (6.0)	-21.1 (7.4)	72.0 (6.9)	233.9 (10.7)	201.0 (12.3)	1907.1 (696.4)	1291.7 (1125.7)	2263.5 (3316.7)	-8.16 (2.46)
3069	15	19	16.7	-8.3 (2.6)	-10.4 (7.5)	-39.6 (8.4)	56.5 (8.3)	257.9 (12.5)	215.8 (12.9)	1672.3 (711.3)	-556.6 (1107.7)	-1410.4 (3941.0)	-16.71 (6.56)
2504	16	20	17.7	-13.3 (2.6)	-29.2 (8.9)	-50.8 (9.2)	53.1 (7.2)	270.2 (12.8)	217.6 (13.4)	1050.0 (750.1)	-1129.9 (1058.7)	-84.7 (4577.8)	-20.35 (7.40)
2013	17	21	18.7	-12.7 (2.8)	-25.2 (10.2)	-59.2 (10.2)	58.5 (6.8)	257.8 (16.5)	218.5 (15.7)	334.5 (786.5)	-1897.6 (1093.2)	-1140.2 (5339.4)	-15.68 (5.60)
1615	18	22	19.7	-15.7 (3.1)	-23.7 (12.7)	-63.7 (11.7)	58.9 (7.4)	284.7 (19.3)	217.0 (19.4)	235.7 (986.6)	-1582.4 (1276.8)	4292.7 (7048.2)	-17.48 (6.75)
1328	19	23	20.7	-14.3 (3.2)	-37.3 (14.3)	-65.4 (13.4)	52.6 (8.5)	298.9 (21.4)	243.7 (21.6)	-1262.7 (1063.2)	-125.2 (1321.9)	10052.2 (7893.0)	-25.89 (11.88)
1093	20	24	21.8	-8.9 (3.6)	-12.4 (17.1)	-62.1 (15.2)	54.4 (9.9)	323.9 (26.8)	241.3 (25.2)	66.4 (1355.4)	-920.7 (1431.5)	3538.6 (8801.9)	-26.59 (13.94)
918	21	25	22.8	-9.9 (4.0)	-26.5 (20.2)	-75.5 (16.7)	48.7 (11.8)	362.1 (28.1)	248.9 (26.8)	1689.7 (1763.6)	462.6 (1537.5)	13621.3 (10629.8)	-39.73 (25.11)
763	22	26	23.7	-2.2 (4.3)	-21.5 (22.2)	-48.2 (18.4)	62.8 (10.4)	329.5 (31.7)	232.4 (34.1)	959.3 (1954.0)	550.4 (1713.7)	7405.9 (12355.0)	-19.61 (10.39)
649	23	27	24.8	-0.9 (4.8)	-12.6 (25.4)	-50.3 (20.7)	85.3 (10.1)	279.1 (46.1)	142.4 (70.0)	1262.5 (2318.5)	873.7 (1984.0)	19147.5 (15005.4)	-5.75 (4.26)
538	24	28	25.8	-1.5 (5.0)	-46.9 (26.9)	-28.4 (23.0)	92.6 (11.4)	191.3 (74.5)	123.6 (112.0)	-1807.9 (2260.6)	2175.8 (2252.1)	26741.0 (16965.0)	-2.02 (3.70)
443	25	29	26.7	-6.1 (5.5)	-36.1 (30.3)	-11.1 (28.0)	90.4 (14.1)	140.5 (138.9)	160.5 (114.7)	-5339.9 (2179.6)	-251.5 (2674.5)	-2283.8 (19133.2)	-1.78 (5.12)